PROCEEDINGS A

royalsocietypublishing.org/journal/rspa

Research

Cite this article: Liu P, Arsuaga J, Calderer MC, Golovaty D, Vazquez M, Walker S. 2022 Helical organization of DNA-like liquid crystal filaments in cylindrical viral capsids. *Proc. R. Soc. A* **478**: 20220047.
https://doi.org/10.1098/rspa.2022.0047

Received: 18 January 2022
Accepted: 6 September 2022

Subject Areas:
applied mathematics, biophysics, materials science

Keywords:
Oseen–Frank theory, liquid crystal, DNA, helical configuration, bifurcation, filament reconstruction

Author for correspondence:
M. Carme Calderer
e-mail: calde014@umn.edu

Downloaded from https://royalsocietypublishing.org/ on 05 October 2022

Helical organization of DNA-like liquid crystal filaments in cylindrical viral capsids

Pei Liu[1,2], Javier Arsuaga[3], M. Carme Calderer[1], Dmitry Golovaty[5], Mariel Vazquez[4] and Shawn Walker[6]

[1]School of Mathematics, University of Minnesota, Twin Cities, MN 55455, USA
[2]Department of Mathematical Sciences, Florida Institute of Technology, Melbourne, FL 32901, USA
[3]Department of Molecular and Cellular Biology, and Department of Mathematics, and [4]Department of Mathematics, and Department of Microbiology and Molecular Genetics, University of California, Davis, CA 95616, USA
[5]Department of Mathematics, University of Akron, Akron, OH 44325, USA
[6]Department of Mathematics, Louisiana State University, Baton Rouge, LA 70803, USA

PL, 0000-0001-8777-6757; MCC, 0000-0002-9117-7439; SW, 0000-0002-8027-5789

We study equilibrium configurations of double-stranded DNA in a cylindrical viral capsid. The state of the encapsidated DNA consists of a disordered inner core enclosed by an ordered outer region, next to the capsid wall. The DNA configuration is described by a unit helical vector field, tangent to an associated centre curve, passing through properly selected locations. We postulate an expression for the energy of the encapsulated DNA based on that of columnar chromonic liquid crystals. A thorough analysis of the Euler–Lagrange equations yields multiple solutions. We demonstrate that there is a trivial, non-helical solution, together with two solutions with non-zero helicity of opposite sign. Using bifurcation analysis, we derive the conditions for local stability and determine when the preferred coiling state is helical.

THE ROYAL SOCIETY PUBLISHING

© 2022 The Author(s) Published by the Royal Society. All rights reserved.

Downloaded from https://royalsocietypublishing.org/ on 05 October 2022

The bifurcation parameters are the ratio of the twist versus the bend moduli of DNA and the ratio between the sizes of the ordered and the disordered regions.

1. Introduction

In this work, we study the packaging geometry of viral double-stranded (ds) DNA of tailed bacteriophages in idealized cylindrical capsids. The cylindrical geometry is taken as a coarse approximation of the actual capsid shapes, including icosahedral and prolate, found in dsDNA bacteriophage viruses [1–7]. These viruses use a molecular motor to store their genome in the protein capsid, where the length of the genome is much larger than the characteristic size of the capsid. We apply data from experimentally characterized viruses, such as the average capsid size and the genome length, to infer properties of the condensed equilibrium states and their bifurcations by taking advantage of the explicit calculations allowed only in the cylindrical geometry. We postpone to future work the treatment of spherical and icosahedral capsids, where numerical approaches are required. We point out that our study does not address single-stranded, helical, RNA viruses, with cylindrical capsids, such as the tobacco mosaic virus [8].

Key stages of the bacteriophage cycle are the phage morphogenesis, which includes capsid assembly and dsDNA packaging, a high pressure quiescent or equilibrium state, and the delivery and infection of the bacterial host. The well-ordered organization of DNA within a viral capsid is essential to ensure efficient genome delivery.

There is an extensive and rich body of work on bacteriophage viruses, involving both imaging techniques and modelling. Leforestier [9] lists three main approaches, the *inverse axial spooling* model, the *ball of yarn* and the *liquid crystalline drop* models. The latter approach stemmed from the evidence gained from X-ray diffraction images of bacteriophages obtained during the 1960s, and later confirmed by cryo-EM microscopy, which provided strong evidence of the *hexagonal* packaging of DNA in the capsid. The liquid crystalline drop model exploits the hexagonal crystal structure locally determined by the points of intersection of the DNA segments on orthogonal planes as experimentally observed. In this approach, hexagonally crystallized monodomains entirely fill the capsid volume, separated by defect walls and forming a structure analogous to the Twist Grain Boundary in a liquid crystal [10,11]. Hexagonal phases have also been observed *in vitro*, with highly concentrated DNA arranged in toroidal clusters [12,13].

In the inverse axial spooling approach, the DNA winds from the capsid periphery to the centre following successive hoops [14,15]. This model and the related DNA arrangement in toroids has been extensively used for several decades [15,16]. Evidence that supports the so-called *spool structural motif* has been provided by the cryo-EM observations of Olson *et al.* [2]. These show that the DNA genome of the phage T4 forms a highly condensed series of concentric layers, spaced about 2.36 nm apart, which tend to follow the contour of the inner wall of the protein capsid. Along these lines, the data obtained by Cerritelli *et al.* [1] suggest that the T7 genome is spooled around the capsid in approximately six coaxial shells in a quasi-crystalline packing. This evidence combined with previous studies of a series of isometric bacteriophages leads to conclude that the coiling organization of condensed DNA may apply to most dsDNA bacteriophages [17]. This underlying model has been used in many different contexts such as the measuring of forces [18] and packaging by molecular motor [19].

Other approaches include a ball of a string and spooling folded toroid [20–23]. The corresponding vector field is tangential to the concentric circles centred on the axis of the cylinder [24,25]. These approaches have been used in the case of spherical-like capsids; in particular, the ball of yarn packages the DNA as in the axial spooling case but following a spherical geometry. One important distinction among the different approaches is the modelling of the core. Information from imaging lacks precision in reference to the structure of the core. In the spooling approach, mostly associated with cylindrical-shaped capsids, the core is simply left empty or filled with strands parallel to the capsid axis.

Downloaded from https://royalsocietypublishing.org/ on 05 October 2022

A common theme in implementing the previous approaches is in that they involve the optimization of an energy functional, very often using tools from Monte Carlo or Brownian motion molecular dynamics. An inherent problem to such approaches is their computational cost, allowing to treat only small genomes. A novel modelling continuum approach is that by Klug & Ortiz [26] based on the introduction of a unit director field, as in nematic liquid crystals, with a scalar variable representing the local density of DNA. An additional feature of the model is the inclusion of a phenomenological *cohesive* energy that penalizes changes of the (hexagonal) cross section. The discretization of the energy, along with the application of the gradient flow method to optimize it, lead to the *torsionless toroidal solenoids*, as the preferred configuration, having lower energy than the inverse spooling structure.

In this paper, we consider the previously introduced continuum model that endows condensed DNA with a structure locally consisting of curvilinear segments (representing the DNA centre axis) together with their orthogonal cross sections [27]. Assigning these segments an effective diameter yields a plane hexagonal crystal structure on the intersecting planes. The capsid core is treated as an isotropic free boundary region representing the disordered state of the DNA. Accordingly, the energy consists of the nematic Oseen–Frank contribution penalizing changes of direction of the vector field (and so that of the DNA axis) and the isotropic energy of the core. Moreover, for the class of helical vector fields (3.3), the former also accounts for the elastic energy associated with the disruption of the hexagonal cross-sectional structure (remark 2.2 and [27]). Furthermore, since images reveal a sharp transition between the ordered and disordered regions of the capsid, we include a surface energy term that tends to minimize the surface area of the interface. One relevant aspect of our approach is that the core is determined by the competition between the bending energy of the ordered region and the isotropic penalty of the core. One relevant aspect of our model is that it allows for twist energy mostly neglected in earlier approaches. Intuitively, it has the effect of releasing bending energy and so affecting the size of the core. However, it does not account for torsion. Mathematically, a key signature of our approach is the vector field-filament structure as in models from nuclear and plasma physics ([28] and the references therein). Although we minimize the energy to obtain the optimal vector field, subsequent integration provides the centre line filament. This also solves the *connectivity* problem affecting the inverse spooling approaches. However, one drawback to our approach is in that the Oseen–Frank energy does not allow for singularities in the vector field (except for point defects in three dimensions). This precludes accounting for the knots often observed in the DNA, an issue that we will address in forthcoming work.

We also depart from earlier works where the DNA is organized in concentric circles, such as in the case of the inverse spooling. Instead, we follow the approach developed to study confinement of semiflexible polymers following helical vector field configurations [29]. In this approach, the unknown vector field $\boldsymbol{n}$ is parameterized by the azimutal angle ψ. In addition to providing connectivity, this approach allows us to incorporate twist deformations, as well as cholesteric effects. The rate of the bending versus twist modulus, $\alpha := K_3/K_2$, turns out crucial in determining how the DNA fills the capsid. Indeed, this parameter provides a quantitative justification for treating condensed DNA as a liquid crystal, and, in particular, endowing it with the Oseen–Frank energy. Values of α used in our work stem from the DNA elasticity and viscosity studies found in [30].

By considering cylindrical capsids of radius R_2 and height $2h$, we obtain an exact expression for the critical values of α. Through a bifurcation analysis, we identify the threshold value of α, below which concentric circles are the optimal organization structure, with helical states above. This result is reminiscent of that in [19] that simulates the filling of a capsid under the axial spooling structure, showing a transition between concentric circles organized as tori to such circles expanding along the capsid axis as the DNA fills the capsid. Our work also admits a natural extension to the case of spheroidal capsids and other general shapes. However, in such cases, the optimization can only be done numerically, although similar patterns of behaviour as for a cylindrical capsid are expected.

Downloaded from https://royalsocietypublishing.org/ on 05 October 2022

We also perform a stability analysis of the solutions and show that the states of four selected viruses fall within the stable helical branches, except for the virus T5, with slightly larger capsid diameter, which is classified within the stable concentric circle branch. The bifurcation structure between concentric circles and helical configurations extends a renowned result on nematic liquid crystals placed between coaxial cylinders [31]. In the latter case, the bifurcation occurs between radial director field configurations and those parallel to the cylindrical axis. From a different point of view, the coexistence between the ordered and disordered DNA regions in the capsid follows the analogous *tactoid* texture phenomenon, observed in small molecule chromonic liquid crystals [32]. The paper concludes with the filament reconstruction. Choosing a point of entrance of the DNA into the capsid, we integrate the vector field along helical segments on the surface of a discrete family of concentric cylinders. The latter are separated by a distance approximately equal to the pitch of the helix. To connect neighbouring helices, an interpolation curve is required at the top and bottom, taking the form of a *U-turn*, heuristically introducing extra bending energy. In order to avoid the latter, an alternative reconstruction connecting helices of opposite handedness would have to be considered. However, this is not a continuous solution to the model. Moreover, the inclusion of the electrostatic energy would be needed for conclusively sorting out between both such configurations. The construction of both connection curves is presented in the electronic supplementary material. The idea of alternating handedness is connected with the helical inversion phenomenon in liquid crystal materials. It has been found, specially in polymer dispersed liquid crystals, in connection with changes of temperature and radiation with ultraviolet light [33]. It is also naturally found in biological systems, although scarcely. For instance, a case remarkably similar to the alternating handedness construction has been reported in the protective tubular structures of the deep-sea worm, where the sign changes every 180° rotation [34]. A comprehensive overview on controlling and understanding the pitch inversion phenomenon is given in [35]. A recent review of viral growth and form can be found in [36]. Our work is also related to those on organization of confined polymers, also models as liquid crystals, both in the achiral and chiral cases [37,38]. Although in the current article we deal with two types of organization, that is, concentric circles and helices, a richer variety of structures has been observed in polymers. Specifically, spontaneous domain formation in spherically confined elastic filaments shows that the ground state of the confined worm-like chain is an ordering mosaic of multiple homogeneously ordered domains, instead of a single spool [39].

The work is organized as follows. In §2, we present the model to be analysed. The main results are developed in §3. In §3a, we consider the case that the inner core radius R_1 is fixed and neglect the energy of the core. Section 3b is devoted to studying the Euler–Lagrange equations of the energy. The zero divergence condition reduces the problem to a nonlinear ordinary differential equation for the angle of orientation of the director field. In §3c, we perform the bifurcation analysis and the investigation of the stability of the different solution branches. Elliptic integrals play a main role in the analysis. In §3d, we treat the core as a free boundary domain and incorporate the isotropic energy in the total form. The section ends with a discussion of the parameters of the model, showing that our results are along the line with actual data, for a set of four sample viruses. Section 4 is devoted to the filament reconstruction for the helices. In §5, we present conclusions and discuss follow up work.

2. The model

In our approach, the equilibrium states of the DNA packaged inside the capsid are associated with those of a unit vector field $\boldsymbol{n}$. The capsid is represented by a bounded, open domain $\mathcal{B}$, consisting of two subsets Ω and Ω_0, whose interiors are disjoint, and such that $\mathcal{B} = \Omega \cup \Omega_0$. The subset Ω represents the region where the DNA is ordered whereas Ω_0 corresponds to the disordered one. In terms of the vector field approach, they represent the nematic and isotropic liquid crystal states, respectively. The unknown fields of the model are the vector field $\boldsymbol{n}$ and the domain Ω_0. We formulate the total energy accordingly, that is, as the sum of the constrained Oseen–Frank energy

royalsocietypublishing.org/journal/rspa Proc. R. Soc. A 478: 20220047

Downloaded from https://royalsocietypublishing.org/ on 05 October 2022

of the nematic plus the isotropic energy of the core region Ω_0. i.e.

$$E = \int_{\Omega} (K_3|\boldsymbol{n} \times \nabla \times \boldsymbol{n}|^2 + K_2(\tau + \boldsymbol{n} \cdot \nabla \times \boldsymbol{n})^2)\, \mathrm{d}\boldsymbol{x} + E_{\text{disorder}}(\Omega_0) \tag{2.1}$$

$$|\boldsymbol{n}| = 1 \quad \text{in } \Omega, \tag{2.2}$$

$$\nabla \cdot \boldsymbol{n} = 0 \quad \text{in } \Omega, \tag{2.3}$$

$$\boldsymbol{n} = \boldsymbol{n}_0 \quad \text{on } \partial\mathcal{B} \cap \partial\Omega \tag{2.4}$$

and

$$\text{Vol}(\Omega) + \text{Vol}(\Omega_0) = \text{Vol}(\mathcal{B}). \tag{2.5}$$

The positive constants K_2 and K_3 denote the twist and bending moduli, respectively, and τ is the chiral pitch. The zero-divergence constraint (2.3) is consistent with the columnar hexagonal nature of the ordered DNA, indicating that the number of filaments that enter an orthogonal unit area cross section also exit it. That is, it guarantees that dislocations do not occur. We now recall a fundamental result in the analysis of the minimization of the Oseen–Frank energy of nematic liquid crystals, with density given by

$$\mathcal{W}_{\text{OF}} = K_1(\nabla \cdot \boldsymbol{n})^2 + K_3|\boldsymbol{n} \times \nabla \times \boldsymbol{n}|^2 + K_2(\tau + \boldsymbol{n} \cdot \nabla \times \boldsymbol{n})^2 + (K_2 + K_4)(\text{tr}(\nabla \boldsymbol{n})^2 - (\nabla \cdot \boldsymbol{n})^2). \tag{2.6}$$

Here, K_1, K_2 and K_3 represent the *splay*, *twist* and *bending* moduli, which have dimensions of force. The following inequalities on the Frank constants K_i, guaranteeing the coercivity of the total energy, play the main role in the analysis:

$$K_1 > 0, \quad K_2 > 0, \quad K_3 > 0, \quad K_2 \geq |K_4|, \quad 2K_1 \geq K_2 + K_4. \tag{2.7}$$

Theorem 2.1. *[40] Let $\mathcal{U} \in \mathbf{R}^3$ be an open and bounded set, with Lipschitz boundary $\partial\mathcal{U}$. Suppose that the Frank constants satisfy the inequalities (2.7). The admissible set $\mathcal{A}(\boldsymbol{n}_0) = \{\boldsymbol{n} \in H^1(\mathcal{U}, \mathcal{S}^2) : \boldsymbol{n}|_{\partial\mathcal{U}} = \boldsymbol{n}_0\}$ is non-empty. Then for any Lipschitz function $\boldsymbol{n}_0 : \partial\mathcal{U} \longrightarrow \mathcal{S}^2$, the functional*

$$E_{OF}(\boldsymbol{n}) := \int_{\mathcal{U}} \mathcal{W}_{OF}(\boldsymbol{n}, \nabla \boldsymbol{n})\, \mathrm{d}\boldsymbol{x} \tag{2.8}$$

admits a minimizer in $\mathcal{A}(\boldsymbol{n}_0)$. Furthermore, if $\boldsymbol{n}$ is a minimizer of $E_{OF}(\cdot)$, then $\boldsymbol{n}$ is analytic in $\mathcal{U}/Z$ for some relatively closed subset Z of $\mathcal{U}$ that has one-dimensional Hausdorff measure zero.

Since the term multiplying $(K_2 + K_4)$ in (2.6) is a null Lagrangian, and given that the boundary conditions imposed on the capsid wall are of Dirichlet type, without loss of generality, we set $K_4 = 0$ and arrive at the expression (§2).

Remark 2.2. The hexagonal columnar phase of chromonic liquid crystals can be characterized by an orthonormal set of vectors $\{\boldsymbol{n}, \boldsymbol{m}, \boldsymbol{p}\}$, the director $\boldsymbol{n}$, the *liquid* direction, describing the average alignment of the columnar axes, and the remaining pair of lattice vectors encoding the geometry of the *crystal* orthogonal cross section. In order to account for the distortion of the lattice, an elastic energy term, $\mathcal{W}_{\text{Hex}}(\boldsymbol{m}, \boldsymbol{p}, \nabla \boldsymbol{m}, \nabla \boldsymbol{p})$, should be added to the integrand of the total energy (2.1). For the class of vector fields $\boldsymbol{n}$ that we consider, including the cross-sectional energy amounts to replacing the constants K_2 and K_3 by effective values that account for the shear and bulk elastic modulus, but it does not otherwise affect the analysis presented here. This simplifying approach may have to be reconsidered if the goal is to predict the osmotic pressure in the capsid [27].

3. Main results

Henceforth, we will take the capsid to be a cylinder of radius $R_2 > 0$ and height $2h$, which in cylindrical coordinates admits the representation $\mathcal{B} = \{(r, z, \theta) | 0 \leq r \leq R_2, 0 \leq \theta < 2\pi, -h \leq z \leq h\}$. For $0 \leq R_1 \leq R_2$, the region where the DNA is organized is expressed as

$$\Omega = \{(r, z, \theta) | R_1 \leq r \leq R_2, 0 \leq \theta < 2\pi, -h \leq z \leq h\}. \tag{3.1}$$

The disordered core is taken to be the inner cylinder $\Omega_0 = \{(r, z, \theta) | 0 \leq r \leq R_1, 0 \leq \theta < 2\pi, -h \leq z \leq h\}$, where R_1, $0 \leq R_1 \leq R_2$, is either a prescribed number or an unknown of the problem. In

royalsocietypublishing.org/journal/rspa Proc. R. Soc. A 478: 20220047

Downloaded from https://royalsocietypublishing.org/ on 05 October 2022

the latter case, we associate with it an energy consistent with the isotropic liquid crystal phase. Specifically, the assigned energy is equal to the sum of two contributions, one proportional to the inner core volume and the second one proportional to the surface area separating the ordered and the disordered regions [27],

$$E_{\text{disorder}}[R_1] = 2h(\nu\pi R_1^2 + 2\sigma\pi R_1). \tag{3.2}$$

Here, $\nu > 0$ is the isotropic modulus and $\sigma \geq 0$ is the surface tension.

We assume the director field $\boldsymbol{n}$ (later identified with the unit tangent vector to the DNA centre curve) takes the form,

$$\boldsymbol{n} = \cos\psi \cdot \boldsymbol{e}_\theta + \sin\psi \cdot \boldsymbol{e}_z, \tag{3.3}$$

where $\psi(r,\theta,z) \in [-\pi/2, \pi/2]$ is a scalar function defined in Ω.

(a) Capsid with prescribed inner core: energy of the ordered region

We will first study the case when $R_1 \geq 0$ is prescribed, neglecting the contribution E_{disorder}. The following theorem refers then to the total Oseen–Frank energy (2.8) of the liquid crystal in the domain Ω, subject to the constraint (2.3).

Theorem 3.1. *Consider the total Oseen–Frank energy (2.8) in the cylindrical shell Ω, with the prescribed inner and outer radii $0 < R_1 < R_2$. Let the Frank constants $K_2, K_3 > 0$ also be given. Suppose that the constraint (2.3) holds and let $\boldsymbol{n}$ be parameterized as in (3.3). Then the critical points of E_{OF} in $H^1(\Omega)$ with natural boundary conditions satisfy the following properties:*

(*i*) *They are independent of θ and z.*
(*ii*) *There exists a smooth (local) energy minimizing configuration $\psi(r)$, $r \in (R_1, R_2)$. Moreover, for achiral energies, $\tau = 0$, $-\psi(r)$ is also a minimizer with the same energy. The scalar fields, $\pm\psi$, determine helical vector fields of opposite handedness.*
(*iii*) *In the case of a chiral material, $\tau \neq 0$, if $\psi(r)$ is a minimizer, then $-\psi(r)$ is also a minimizer of E_{OF} with the chiral pitch $-\tau$.*

Proof. For $\boldsymbol{n}$ of the form (3.3), the Oseen–Frank energy reduces to

$$E_{\text{OF}} = \int_\Omega \left[K_3 \left(\left(\frac{\cos^2\psi}{r} \right)^2 + \left(\frac{\cos^2\psi}{r}\psi_\theta + \frac{\sin(2\psi)}{2}\psi_z \right)^2 + \left(\frac{\sin(2\psi)}{2r}\psi_\theta + \sin^2\psi\,\psi_z \right)^2 \right) + K_2 \left(\frac{\sin(2\psi)}{2r} - \psi_r + \tau \right)^2 \right] \mathrm{d}\boldsymbol{x}. \tag{3.4}$$

The constraint $\nabla \cdot \boldsymbol{n} = 0$ becomes

$$\psi_z = \frac{\tan\psi}{r}\psi_\theta. \tag{3.5}$$

Substituting the latter into the Oseen–Frank energy, it further simplifies to

$$E_{\text{OF}}[\psi(r,\theta,z)] = \int_\Omega \left[K_3 \left(\left(\frac{\cos^2\psi}{r} \right)^2 + \frac{1}{r^2\cos^2\psi}\psi_\theta^2 \right) + K_2 \left(\frac{\sin(2\psi)}{2r} - \psi_r + \tau \right)^2 \right] \mathrm{d}\boldsymbol{x} \tag{3.6}$$

$$\geq \int_\Omega \left[K_3 \left(\frac{\cos^2\psi}{r} \right)^2 + K_2 \left(\frac{\sin(2\psi)}{2r} - \psi_r + \tau \right)^2 \right] \mathrm{d}\boldsymbol{x} \tag{3.7}$$

$$= \int_{-h}^{h} \int_0^{2\pi} \int_{R_1}^{R_2} \left[K_3 \left(\frac{\cos^2\psi}{r} \right)^2 + K_2 \left(\frac{\sin(2\psi)}{2r} - \psi_r + \tau \right)^2 \right] r\,\mathrm{d}r\,\mathrm{d}\theta\,\mathrm{d}z \tag{3.8}$$

$$\triangleq E_{\text{order}}[\psi(r,\theta,z)]. \tag{3.9}$$

Downloaded from https://royalsocietypublishing.org/ on 05 October 2022

We point out that a critical point of $E_{\text{order}}[\psi(r,\theta,z)]$, which satisfies $\delta E_{\text{order}}/\delta\psi = 0$, where the symbol δ refers to the total variation of E_{OF} with respect to $\psi(r)$, satisfies

$$-K_2[(r\psi_r)]_r + \frac{\sin(2\psi)}{2r}(K_2\cos(2\psi) - 2K_3\cos^2\psi) = \tau(\cos(2\psi)+1). \tag{3.10}$$

The boundary conditions also result from setting the first variation of the energy equal to zero, that is,

$$2r\psi_r \pm \sin(2\psi) = 0 \quad \text{or} \quad \psi = C, \tag{3.11}$$

at $r = R_1$ and $r = R_2$, where C is a suitably chosen constant. Here the '+' sign corresponds to $r = R_1$ and the '−' sign to $r = R_2$. The difference of signs is due to the opposite directions of the outer normal at two different boundary components.

In general, the solution to (3.10) and (3.11) may depend on (θ, z) as parameters. However, the solution, which corresponds to the energy minimizer, is independent of θ and z, thus

$$E_{\text{order}}[\psi(r,\theta,z)] \geq E_{\text{order}}[\psi(r)]. \tag{3.12}$$

We observe the critical points of the energy, that is, solutions of the Euler–Lagrange equation (3.10), are smooth functions. It follows from standard theory of ordinary differential equations [41]. ■

Remark 3.2. Theorem 3.1 relies on the cylindrical geometry. If we consider the spherical domain, then the Oseen–Frank energy is minimized with ψ dependent on all three coordinates r, θ and z.

In view of theorem 3.1, from now on we will only consider axisymmetric solutions $\psi(r)$. We also note that there exists a constant trivial solution to equation (3.10), which is $\psi = \pi/2$. It describes the configuration of the director field to be parallel straight lines pointing from the bottom to the top, corresponding to the spiral-fold model [42], which is not discussed in this paper. If we further assume the chirality $\tau = 0$, then $\psi = 0$ is also a constant trivial solution, which describes the director field tangent to concentric circles.

In what follows, we first discuss the case $\tau = 0$; we will return to configurations with non-zero chirality in later sections. For physical consistency, we impose the natural boundary condition at R_1: $2R_1\psi_r(R_1) + \sin(2\psi(R_1)) = 0$, and the Dirichlet condition at R_2: $\psi(R_2) = 0$. This set-up describes a liquid crystal, with the director field circularly anchored to the outer surface and free on the inner one. The concentric-circle configuration can be viewed as a two-dimensional liquid crystal structure, while the three-dimensional helical configuration corresponds to non-constant $\psi(r) \neq 0$. The transition from the concentric-circle to helical solutions is a type of 'escape to the third dimension' in nematic liquid crystals confined to cylinders [43].

We first study the existence of the helical solution and the stability of, both, the concentric-circle and helical solutions, under different sets of parameters.

(b) Solution of the Euler–Lagrange equations

We consider the governing equation (3.10), with $\tau = 0$, subject to the boundary conditions

$$\begin{cases} 2r\psi_r + \sin(2\psi) = 0, & \text{at } r = R_1; \\ \psi = 0, & \text{at } r = R_2. \end{cases} \tag{3.13}$$

We observe that the trivial solution $\psi(r) = 0$ satisfies both boundary conditions, with the corresponding vector field $\boldsymbol{n}$ being tangent to concentric circles.

Downloaded from https://royalsocietypublishing.org/ on 05 October 2022

Next, we focus on non-trivial solutions $\psi \neq 0$, with $\boldsymbol{n}$ tangent to families of helical curves. For this, we introduce the parameter

$$\alpha = \frac{K_3}{K_2}, \tag{3.14}$$

which will turn out to be pivotal in classifying the solutions of the equation. We first note that, integrating both sides of equation (3.10), after pre-multiplying by ψ_r, yields the first integral

$$(r\psi_r)^2 - \frac{\alpha}{2}\cos(2\psi) - \frac{1-\alpha}{8}\cos(4\psi) = C, \tag{3.15}$$

with C being an arbitrary constant. Using the boundary condition at $r = R_1$, the constant C can be expressed as

$$C = \frac{1}{4}\sin^2(2\psi(R_1)) - \frac{\alpha}{2}\cos(2\psi(R_1)) - \frac{1-\alpha}{8}\cos(4\psi(R_1)). \tag{3.16}$$

Equation (3.15) can be integrated once more.

The solution satisfying the boundary condition $\psi(R_2) = 0$, is given by the elliptic integral

$$\frac{F\left(\arcsin\left(\sqrt{m_2/(1-m_2)}\tan\psi\right)\middle|\,(m_1(1-m_2))/(m_2(1-m_1))\right)}{\sqrt{(1-\alpha)(1-m_1)m_2}} = \pm\ln\frac{R_2}{r}. \tag{3.17}$$

Here, $F(x|m) = \int_0^x \left(\mathrm{d}\theta/\sqrt{1-m\sin^2\theta}\right)$ is the elliptic integral of the first kind, with

$$m_{1,2} = \frac{(1-2\alpha)/2 \pm \sqrt{\alpha^2/4 + (1-\alpha)^2/8 - (1-\alpha)C}}{1-\alpha}.$$

A detailed derivation of (3.17) is given in the electronic supplementary material section.

To determine the constant C or, equivalently, $\psi(R_1)$, we need to consider the boundary condition (3.13) at R_1 and solve the resulting equation

$$\frac{F\left(\arcsin\left(\sqrt{m_2/(1-m_2)}\tan\psi(R_1)\right)\middle|\,m_1(1-m_2)/m_2(1-m_1)\right)}{\sqrt{(1-\alpha)(1-m_1)m_2}} = \pm\ln\frac{R_2}{R_1} \triangleq \pm M. \tag{3.18}$$

We note that $\psi(R_1)$ depends on R_2 through the ratio R_2/R_1 only, and $M \triangleq \ln(R_2/R_1)$ turns out to be an important parameter in later sections.

We observe that, when $R_1 \to 0$ with fixed R_2, or when $\alpha \to 1$, equation (3.18) may not be properly defined. The first case corresponds to the DNA being fully ordered in the whole capsid, whereas the second one corresponds to the limit of equal twist and bending effects. Next, let us carefully analyse these two special cases, and then the general situation.

(i) $R_1 = 0$

The energy of the system reduces to

$$E_{\text{order}} = 4\pi h K_2 \int_0^{R_2} \left[\left|\frac{\sin(2\psi)}{2r} - \psi_r\right|^2 + \alpha\frac{\cos^4\psi}{r^2}\right] r\,\mathrm{d}r. \tag{3.19}$$

The boundary condition $2r\psi_r + \sin(2\psi) = 0$ at $r = 0$ indicates $\psi(0) = 0$ or $\pi/2$.

If $\psi(0) = 0$, the first integral becomes

$$(r\psi_r)^2 = -\alpha\sin^2(\psi) - \frac{1-\alpha}{4}\sin^2(2\psi). \tag{3.20}$$

We point out that, for given $K_2, K_3 > 0$, the right-hand side of the previous equation is non-positive. Thus, only the trivial solution $\psi(r) = 0$ exists.

Downloaded from https://royalsocietypublishing.org/ on 05 October 2022

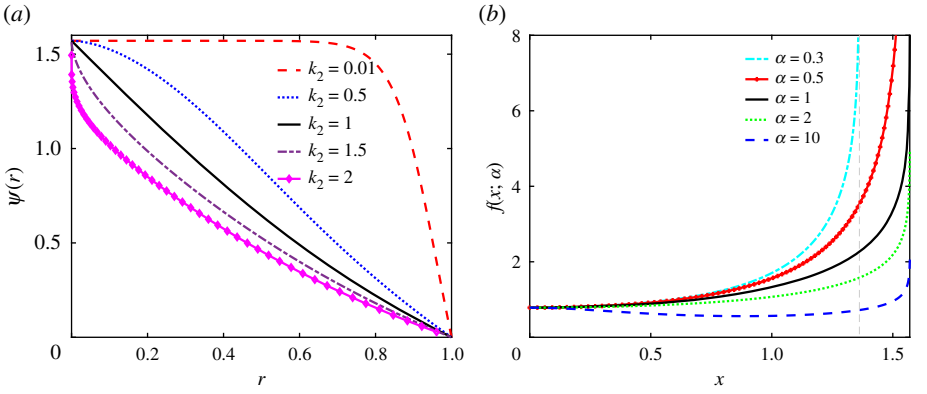

Figure 1. (*a*) Solution $\psi(r)$ given by equation (3.22), with $R_1 = 0$, $R_2 = 1$, $K_3 = 1$ and different K_2. (*b*) The graph of function $f(x;\alpha)$ for different values of α. The curves with $\alpha = 0.5, 1, 2, 10$ have a vertical asymptote at $x = \pi/2$. The vertical asymptote for $\alpha = 0.3$ is $x = \beta(\alpha) < \pi/2$. The curves with $\alpha = 0.3, 0.5, 1, 2$ are monotonically increasing, while the curve for $\alpha = 10$ is decreasing then increasing. (Online version in colour.)

Next, we focus on the case that $\psi(0) = \pi/2$. The first integral (3.15) and (3.16) becomes

$$(r\psi_r)^2 = \alpha\cos^2(\psi) - \frac{1-\alpha}{4}\sin^2(2\psi). \tag{3.21}$$

Integrating it once more, we get

$$\frac{1}{\sqrt{2\alpha-1}}\tanh^{-1}\left(\frac{\sqrt{2\alpha-1}\sin(\psi)}{\sqrt{2\alpha-1+(1-\alpha)\cos^2\psi}}\right) = \pm\ln\frac{r}{R_2}, \tag{3.22}$$

which implicitly defines the function $\psi(r)$. In the special case $\alpha = 1$, it becomes

$$\psi = \pm\arcsin\frac{R_2^2 - r^2}{R_2^2 + r^2} = \pm\arccos\frac{2rR_2}{R_2^2 + r^2}. \tag{3.23}$$

Likewise, for $\alpha = 1/2$, the explicit form of the solution is

$$\psi = \pm\arctan\left(\frac{\ln(R_2/r)}{\sqrt{2}}\right). \tag{3.24}$$

The graphs of $\psi(r)$, for different values of α, are shown in figure 1*a*.

Remark 3.3. (a) For $\alpha < 1/2$, equation (3.22) does not have real solutions, indicating that the boundary conditions in (3.13) fail. Hence only the solutions with $\boldsymbol{n}$ tangent to concentric circles exist. (b) For $\alpha \geq 1/2$, the configurations given by (3.22) have finite energy, E_{order}, and it is independent of R_2. (See the electronic supplementary material for the proof.)

(ii) $\alpha = 1$ with $R_1 > 0$

In this special case, the first integral becomes

$$(r\psi_r)^2 - \frac{1}{2}\cos(2\psi) = C. \tag{3.25}$$

Using the boundary condition at $r = R_1$, then $C = (\sin^2(2\psi(R_1))/4) - \frac{1}{2}\cos(2\psi(R_1))$, and

$$r\psi_r = \pm\sqrt{\frac{C + \cos(2\psi)}{2}}. \tag{3.26}$$

Downloaded from https://royalsocietypublishing.org/ on 05 October 2022

Integrating (3.25) again and applying the boundary condition $\psi(R_2)=0$, we have

$$\frac{1}{\sqrt{m}}F(\psi|\frac{1}{m})=\pm\ln\frac{r}{R_2}. \tag{3.27}$$

Here, $m=C+\frac{1}{2}=(\sin^2(2\psi(R_1))/4)+\sin^2(\psi(R_1))$, and $F(x|m)=\int_0^x\left(\mathrm{d}\theta/\sqrt{1-m\sin^2\theta}\right)$ is the elliptic integral of the first kind.

In order to determine $\psi(R_1)$, we need to solve the following equation:

$$\frac{1}{\sqrt{m}}F\left(\psi(R_1)|\frac{1}{m}\right)=\pm M. \tag{3.28}$$

Let us define

$$\begin{aligned} f(x)&\triangleq\frac{2F(x|(4/(\sin^2(2x)+4\sin^2(x))))}{\sqrt{\sin^2(2x)+4\sin^2(x)}}\\ &=\frac{2x}{\sqrt{\sin^2(2x)+4\sin^2(x)}}\int_0^1\frac{\mathrm{d}u}{\sqrt{1-(4\sin^2(xu)/(\sin^2(2x)+4\sin^2(x)))}}. \end{aligned} \tag{3.29}$$

This allows us to rewrite equation (3.28) as $f(\psi(R_1))=\pm M$, with M as in (3.18). The results of this subsection are summarized in the following theorem and the proof can be found in the electronic supplementary material.

Theorem 3.4. *Let $\alpha=1$ in equation (3.14). Then there exists a unique positive solution $\psi(R_1):=c>0$ to equation (3.28) if and only if $R_2/R_1>\mathrm{e}^{\pi/4}\approx 2.19328$. Likewise, $\psi(R_1)=-c<0$ is the only negative solution. Furthermore, the functions $\psi(r)$ given by equation (3.27), with $\psi(R_1)=\pm c$, are the only two non-trivial solutions of equation (3.10) satisfying the boundary conditions (3.13).*

Remark 3.5. (a) For $R_2/R_1=\mathrm{e}^{\pi/4}$, we define $f(0)=\lim_{x\to 0}f(x)=\pi/4$. Then equation (3.27) has a solution satisfying $\psi(R_1)=0$, which corresponds to the trivial solution $\psi(r)\equiv 0$. (b) When $R_1\to 0$, so that $R_2/R_1\to\infty$, the solution $\psi(r)$ satisfies $\psi(R_1)\to\pi/2$. This is consistent with the result from §i.

(iii) General cases

Now we revisit equation (3.10), and analyse the general case $\alpha\geq 0$ and $R_1>0$ prescribed. Instead of formally using the elliptic integral, we start again from the first integral, and consider the function,

$$\begin{aligned} f(x;\alpha)&=\int_0^x\frac{\mathrm{d}t}{\sqrt{(\alpha/2)(\cos(2t)-\cos(2x))+((1-\alpha)/8)(\cos(4t)-\cos(4x))+\frac{1}{4}\sin^2(2x)}}\\ &=\int_0^1\frac{x\,\mathrm{d}u}{\sqrt{(1-\alpha)\sin^4(xu)-\sin^2(xu)+2\sin^2(x)-(2-\alpha)\sin^4(x)}}. \end{aligned} \tag{3.30}$$

Note that $f(x;\alpha=1)$ is the same function of x as $f(x)$ in equation (3.29). By definition, and in analogy with equation (3.28), equation (3.18) can be rewritten as

$$f(\psi(R_1);\alpha)=\pm M=\pm\ln\frac{R_2}{R_1}. \tag{3.31}$$

The properties of f give us sufficient information on the solution $\psi(r)$. Furthermore, since $f(x;\alpha)$ is an odd function of x, we only need to consider the positive sign in equation (3.31). Let us define,

$$G(u,x;\alpha)=(1-\alpha)\sin^4(xu)-\sin^2(xu)+2\sin^2(x)-(2-\alpha)\sin^4(x), \tag{3.32}$$

for $x\in[0,\pi/2]$ and $u\in[0,1]$. Note that G is continuously differentiable with respect to both x and u. With x fixed, $G(u,x;\alpha)$ can be viewed as a function of u only. We now discuss the properties of

Downloaded from https://royalsocietypublishing.org/ on 05 October 2022

G and f, for two distinct ranges of values of α, that is, $\alpha \geq \frac{1}{2}$ and $\alpha < \frac{1}{2}$. The conclusions are based on calculating the derivative of G with respect to u.

When $\alpha \geq 1/2$, there is no interior critical point with respect to u, thus the extreme values of G can only occur at the end points $u = 0$ or $u = 1$. Moreover, it is easy to check that $G(0, x; \alpha) > 0$ and $G(1, x; \alpha) > 0$, for all $x \in (0, \pi/2)$, and so $G(u, x; \alpha) > 0$ for all $x \in (0, \pi/2)$ and $u \in [0, 1]$. Hence $f(x; \alpha)$ is properly defined as a real function in $0 < x < \pi/2$. We can further calculate the limit,

$$\lim_{x \to \pi/2} f(x; \alpha) = \infty, \quad \text{if } \alpha \geq \frac{1}{2}. \tag{3.33}$$

When $\alpha < 1/2$, there is no interior critical point of G with respect to u, for $x \in (0, x_0]$, with $x_0 = \arcsin\left(\sqrt{1/(2 - 2\alpha)}\right)$. Thus the arguments used for the case $\alpha \geq \frac{1}{2}$ still hold; hence $f(x; \alpha)$ is a real function in $(0, x_0]$. For $x \in (x_0, \pi/2)$, there is one interior critical point of $G(u, x; \alpha)$, that is, $u_0 = x_0/x$. Since $G(u_0(x), x; \alpha)$ is monotonically decreasing in $x \in [x_0, \pi/2]$, $G(1, x_0; \alpha) > 0$ and $G(2x_0/\pi, \pi/2; \alpha) < 0$, there must exist one $\beta \in (x_0, \pi/2)$, such that $G(u_0(x), x; \alpha) < 0$ for all $x \in (\beta, \pi/2)$ and $G(u_0(x), x; \alpha) > 0$ for all $x \in (x_0, \beta)$. When $x \in (\beta, \pi/2)$, $f(x; \alpha)$ becomes complex because $\sqrt{G(u, x; \alpha)}$ is pure imaginary near $u = u_0(x)$. When $x \in (0, \beta)$, $f(x; \alpha)$ is real. For $x = \beta$, since $G(x_0/\beta, \beta; \alpha) = G_u(x_0/\beta, \beta; \alpha) = 0$, the integral $\int G^{-1/2}\, \mathrm{d}u$ diverges, thus

$$\lim_{x \to \beta} f(x; \alpha) = \infty, \quad \text{if } \alpha < \frac{1}{2}. \tag{3.34}$$

In both cases, $\alpha \geq 1/2$ and $\alpha < 1/2$, we get the common limit

$$\lim_{x \to 0} f(x; \alpha) = \int_0^1 \frac{\mathrm{d}u}{\sqrt{2 - u^2}} = \frac{\pi}{4}. \tag{3.35}$$

Proceeding with the Taylor expansion of $f(x; \alpha)$ about $x = 0$, we get higher-order corrections to the previous limit, i.e.

$$\begin{aligned} f(x; \alpha) &\sim \int_0^1 \left(1 - \frac{(1 - \alpha)u^4 + u^4/3 - 2/3 + (\alpha - 2)}{4 - 2u^2} x^2\right) \frac{\mathrm{d}u}{\sqrt{2 - u^2}} \\ &= \frac{\pi}{4} - x^2 \left(\frac{2 - \pi}{2} + \frac{3\pi - 8}{8}\alpha\right). \end{aligned} \tag{3.36}$$

Hence, it follows that $f'(0; \alpha) = 0$, and $f''(0; \alpha) > 0$, when $\alpha < (4\pi - 8)/(3\pi - 8)$; $f''(0; \alpha) < 0$, when $\alpha > (4\pi - 8)(3\pi - 8)$. The graphs of $f(x; \alpha)$, for different values of α, are shown in figure 1*b*.

Remark 3.6. Numerical calculations show that $f(x; \alpha)$ is monotonically increasing when $\alpha \leq ((4\pi - 8)/(3\pi - 8))$, and $f(x; \alpha)$ has one local minimum when $\alpha > (4\pi - 8)/(3\pi - 8)$.

We point out that, for α small, $f(x; \alpha)$ is monotonically increasing. For α large, $f(x; \alpha)$ has an interval of decrease followed by one of increase, as x grows. Here, we omit the detailed calculation of the study of the monotonicity of $f(x; \alpha)$. Since it is very tedious, and instead we refer the reader to the numerical calculations shown in figure 1. We summarize the previous results as follows:

(i) When $0 \leq \alpha < 1/2$, then $f(x; \alpha)$ is a real, monotonically increasing function in $(0, \beta(\alpha)) \subset (0, \pi/2)$, whose range is $(\pi/4, \infty)$. A non-trivial solution to equation (3.31) exists if $M > \pi/4$, and the solution is unique.

(ii) When $\alpha \geq 1/2$, then $f(x; \alpha)$ is real in $(0, \pi/2)$. If $f(x; \alpha)$ is monotonically increasing, then its range is $(\pi/4, \infty)$, and a non-trivial solution to equation (3.31) exists if $\ln(R_2/R_1) > \pi/4$; the solution is unique. If $f(x; \alpha)$ is not monotonic, then its range is $[a, \infty)$ for some $a < \pi/4$. A non-trivial solution to equation (3.31) exists if $M = \ln(R_2/R_1) > a$, and the solution is not unique if $a < M < \pi/4$. We point out that a is the minimum of $f(x; \alpha)$.

(iii) In all cases, the non-trivial solution $\psi(r)$ depends on R_2 only through the ratio R_2/R_1. Likewise, the dependence on the elasticity constants is solely through the ratio $\alpha = K_3/K_2$.

Downloaded from https://royalsocietypublishing.org/ on 05 October 2022

(c) Stability of solutions

(i) Local stability of the helical solution $\psi(r)$

We consider a small perturbation $\delta\psi(r) \in H_0^1([R_1, R_2])$ about the helical solution $\psi(r)$. Ignoring the higher-order terms, it changes the energy by the amount

$$\delta E_{\text{order}} = 4\pi h K_2 \int_{R_1}^{R_2} [[\cos(2\psi)\delta\psi - r\delta\psi_r]^2 - [\sin(2\psi) - 2r\psi_r]\sin(2\psi)(\delta\psi)^2 + 6\alpha\cos^2\psi\sin^2\psi(\delta\psi)^2 - 2\alpha\cos^4\psi(\delta\psi)^2]\frac{\mathrm{d}r}{r}.$$

Let $x = \ln r - \ln R_1$ and recall that $M = \ln R_2 - \ln R_1$. Then

$$\delta E_{\text{order}} = 4\pi h K_2 \int_0^M \left[(\delta\psi_x)^2 + [\cos(4\psi) + \frac{3\alpha}{2}\sin^2(2\psi) - 2\alpha\cos^4\psi](\delta\psi)^2\right]\mathrm{d}x, \tag{3.37}$$

$$\geq 4\pi K_2 h \int_0^M \left[\cos(4\psi) + \frac{3\alpha}{2}\sin^2(2\psi) - 2\alpha\cos^4\psi + \frac{\pi^2}{M^2}\right](\delta\psi)^2\,\mathrm{d}x. \tag{3.38}$$

Here, we applied Wirtinger's inequality. The equality holds when $\delta\psi \propto \sin(\pi x/M)$. This allows us to establish the following theorem, whose proof can be found in the electronic supplementary material.

Theorem 3.7. *The helical solution $\psi(r)$ is stable in the following cases:*

(i) *If $0 \leq \alpha \leq \frac{4}{5}$, when $M = \ln(R_2/R_1) \leq \pi/\sqrt{1 - \alpha + (\alpha^2/8(1-\alpha))}$;*

(ii) *If $\alpha > \frac{4}{5}$, when $M = \ln(R_2/R_1) \leq \pi/\sqrt{2\alpha - 1}$.*

(ii) Local stability of the concentric-circle solution $\psi = 0$

Let us consider a small perturbation $\delta\psi(r) \in H_0^1([R_1, R_2])$ about the solution $\psi(r) = 0$. Ignoring the higher-order terms, the corresponding change in the energy is

$$\delta E_{\text{order}} = 4\pi h K_2 \int_0^M [(1-2\alpha)(\delta\psi)^2 + (\delta\psi_x)^2]\,\mathrm{d}x \geq 4\pi h K_2 \int_0^M \left[1 - 2\alpha + \frac{\pi^2}{M^2}\right](\delta\psi)^2\,\mathrm{d}x.$$

We now establish the following theorem, whose proof is given in the electronic supplementary material.

Theorem 3.8. *The concentric-circle solution $\psi(r) = 0$ has the following properties:*

(*i*) *It is stable, provided $0 \leq \alpha \leq 1/2$; or $\alpha > 1/2$ and $M = \ln(R_2/R_1) < \pi/\sqrt{2\alpha - 1}$.*
(*ii*) *It is unstable, if $\alpha > 1/2$ and $M = \ln(R_2/R_1) > \pi/\sqrt{2\alpha - 1}$.*

Remark 3.9. Theorems 3.7 and 3.8 show that both the concentric and helical solutions are stable when the ordered region has a large radius. Moreover, when bending is relatively weak, the concentric solution is always stable. In the case that the concentric solution is unstable, we expect the helical solution to be stable, although it may not satisfy the sufficient (but not necessary) conditions of theorem 3.7.

(iii) Energy comparison

We now compare the energy of the concentric circle solution with that of the helical one. The former can be explicitly calculated as

$$E_{\text{order}}[\psi(r) = 0] = 4\pi h K_2 \alpha \int_{R_1}^{R_2} \frac{1}{r}\,\mathrm{d}r = 4\pi h K_2 \alpha \ln\frac{R_2}{R_1}. \tag{3.39}$$

Downloaded from https://royalsocietypublishing.org/ on 05 October 2022

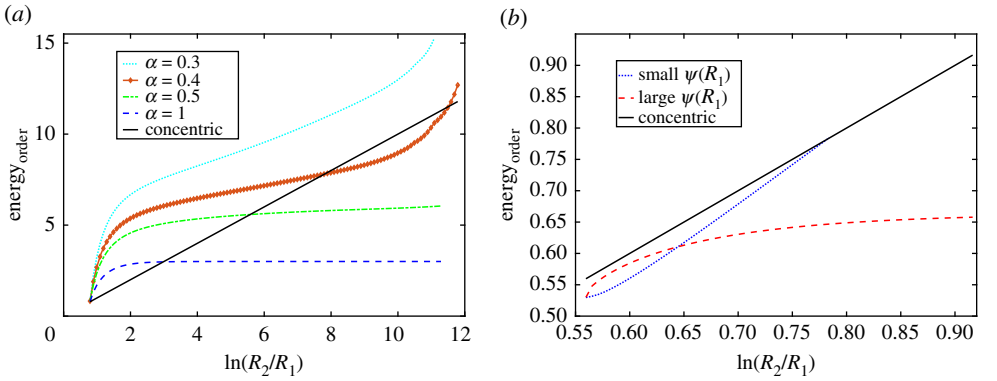

Figure 2. Total energy of the system for different configurations and parameter values. In both graphs, the black line is the plot of the energy of the concentric circle configuration. The coefficient $4\pi hK_3$ is omitted for all the curves. (*a*) The plot of the helical configurations for $\alpha = 0.3, 0.4, 0.5$ and 1. Panel (*b*) corresponds to $\alpha = 10$. There are two helical solutions with different positive $\psi(R_1)$. The figure shows the energy of both helical configurations. (Online version in colour.)

For the helical solutions, the energy has to be numerically calculated. Notice that the energy only depends on the ratio R_2/R_1: figure 2 shows the comparisons between the energies as a function of $M = \ln(R_2/R_1)$ for different values of α. We set $K_3 = 1$ and let K_2 change.

The α values in (*a*) correspond to the situation when there is only one positive solution $\psi(R_1)$ of (3.31). When $\alpha = 0.3$, the concentric-circle solution is preferred because it has a lower energy than the helical configuration.

When $\alpha = 0.4$, the helical configuration has a lower energy for a limited range of M. These two curves show that, when $M \to \infty$, the energy diverges faster than that of the concentric-circle configuration. This is consistent with remark 3.3. When $\alpha = 0.5$ and 1, the helical solution has a higher energy for smaller M and becomes preferable for large R_2/R_1. Moreover, these two curves become horizontal when $M \to \infty$, which is also consistent with the statement in remark 3.3.

In the figures of panel (*b*), α is set to be equal to 10. We have shown in figure 1 that there exist two positive solutions of $\psi(R_1)$ for a particular range of $a < M < \pi/4$. One is marked as small $\psi(R_1)$ and the other as large $\psi(R_1)$. In the case $M \to a^+$, the two helical solutions become identical. When $M \to (\pi/4)^-$, the small $\psi(R_1)$ solution degenerates to the trivial concentric-circle solution, thus the small $\psi(R_1)$ branch vanishes when $M < a$ or $M > \pi/4$. The solution corresponding to large $\psi(R_1)$ exists for $M \geq a$. We note that the helical configuration in this case is always preferred compared with the concentric-circle configuration. Moreover, the small $\psi(R_1)$ branch is preferred when M is small; the large $\psi(R_1)$ branch is preferred when M is large. However, at the (right) intersection of the two energy curves of the helical configurations, the values of $\psi(R_1)$ are distinct. This suggests that the phase transition between these two helical configurations, as M changes through the threshold value, is not smooth.

(d) Capsid with core energy: variable R_1 with fixed R_2

Next, we consider the total energy that consists of the sum of the ordered plus the disordered contributions, with the unknown fields being $\psi = \psi(r)$ and the real number $R_1 \geq 0$

$$E_{\text{total}}[\psi, R_1] = E_{\text{disorder}}[R_1] + E_{\text{order}}[\psi]$$
$$= 2\pi h \left[\nu R_1^2 + 2\sigma R_1 + 2\int_{R_1}^{R_2} \left(K_2 \left| \frac{\sin(2\psi)}{2r} - \psi_r + \tau \right|^2 + K_3 \frac{\cos^4 \psi}{r^2} \right) r\mathrm{d}r \right]. \quad (3.40)$$

Downloaded from https://royalsocietypublishing.org/ on 05 October 2022

Note that $E_{\text{order}}[\psi]$ also depends on R_1. The critical points satisfy the equations

$$\frac{\delta E_{\text{total}}}{\delta \psi} = 0 = \frac{\partial E_{\text{total}}}{\partial R_1}. \tag{3.41}$$

It follows that the governing equation for $\psi(r)$ and the corresponding boundary conditions are again given by equations (3.10) and (3.11), respectively. The second equation in (3.41) gives the relation satisfied by the unknown quantity R_1,

$$\nu R_1 + \sigma = \left[K_2 \left| \frac{\sin(2\psi(R_1))}{2R_1} - \psi_r(R_1) + \tau \right|^2 + K_3 \frac{\cos^4 \psi(R_1)}{R_1^2} \right] R_1. \tag{3.42}$$

We will again consider the case $\tau = 0$ and substitute the natural boundary conditions (3.11) into (3.42) yielding the equation

$$\nu R_2^2 \frac{R_1}{R_2} + \sigma R_2 = g\left(\frac{R_1}{R_2}\right) \triangleq K_2 \frac{\sin^2(2\psi(R_1))}{R_1/R_2} + K_3 \frac{\cos^4 \psi(R_1)}{R_1/R_2}. \tag{3.43}$$

Here, we used the fact that $\psi(R_1)$ only depends on the ratio R_1/R_2, determined by equation (3.18) or (3.31). Thus R_1/R_2 (or equivalently R_1) and $\psi(R_1)$ could be obtained through a set of algebraic equations, without solving the boundary value problem (3.10) and (3.11).

Remark 3.10. Before discussing the solvability of equation (3.43), we carry out a simple calculation that gives insight to the possible structure of solutions, according to the parameter values. Introducing the variable $z = \cos^2 \psi(R_1)$, we rewrite the former as a quadratic equation on z,

$$\nu R_1 + \sigma = (1/R_1)[Nz^2 + 4K_2 z], \quad N := (K_3 - 4K_2). \tag{3.44}$$

Solving it provides a relationship between $\cos^2 \psi(R_1)$ and R_1, according to the sign of N. Specifically, (a) there is a single branch relationship between z and R_1, provided $N \geq 0$ (equivalently, $\alpha \geq 4$), and (b) two possible branches otherwise (i.e. $\alpha < 4$).

(i) Determine the inner core radius R_1

We now discuss the numerical solution of equation (3.43). In figure 3, we represent the graphs of the function $g(R_1/R_2)$ in equation (3.43), for $\psi(R_1)$ corresponding to concentric circle vector fields as well as to helical ones, and for several choices of the parameter α. These curves illustrate all possible shapes of $g(R_1/R_2)$. Solutions of equation (3.43) are then given by intersections of such curves with the line $\nu R_2^2(R_1/R_2) + \sigma R_2$. We observe that, given a pair (ν, σ) for which an intersection with a graph of $g(R_1/R_2)$ with negative slope occurs, subsequent increase of σ, with ν fixed, causes the value of R_1 at the intersection to decrease; this is also the case when ν increases while keeping σ fixed. We also observe that, if on the left of the location of the intersection the straight line is above the curve of g, the energy increases with increasing R_1; otherwise, the energy decreases with increasing R_1.

We now summarize the solvability of equation (3.43) as follows.

For the concentric-circle curve: (1) In the case of no intersection (corresponding to small ν and σ), then the stable configuration is $R_1 = 1$, with the full inner capsid region being disordered; (2) if there is one intersection, then the concentric-circle configuration is stable in R_1.

For $\alpha = 0.5$: (1) if there is an intersection, then the helical configuration is stable in R_1; (2) if there is no intersection, then the stable configuration is determined by the concentric-circle curve.

For $\alpha = 1.5$: there might be two intersections, (1) the helical configuration with $R_1 = 0$ is stable in R_1; (2) if there is one intersection where the straight line crosses the curve from above, then it is unstable; (3) if there is one intersection where the straight line crosses the curve from below, then it is stable in R_1.

For $\alpha = 3$: (1) the helical configuration with $R_1 = 0$ is stable in R_1; (2) if there is an intersection, then the helical configuration is unstable in R_1.

For $\alpha = 10$, there are two branches of curves: (1) the helical configuration with $R_1 = 0$ is stable in R_1; (2) if there is one intersection with the lower curve, then it is unstable. The configuration

Downloaded from https://royalsocietypublishing.org/ on 05 October 2022

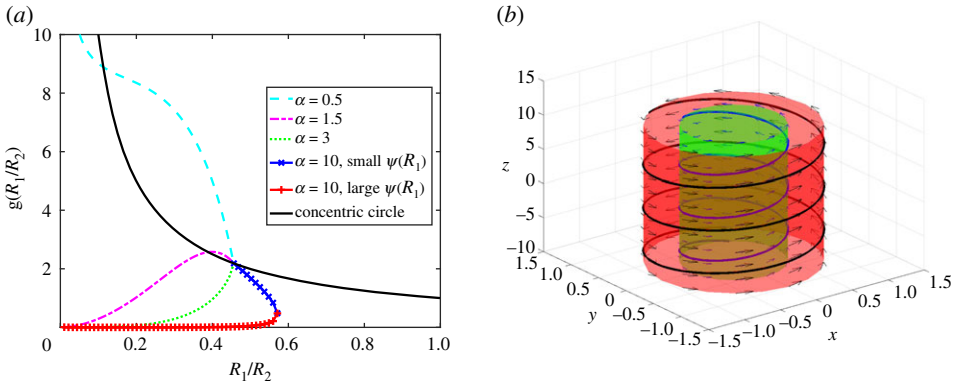

Figure 3. (*a*) Plot of the function $g(R_1/R_2)$ of equation (3.43) corresponding to concentric circle vector fields (black line) and to helical vector fields. The purple curve shows that, for suitable values of ν and σ, two solutions R_1 exist for $\alpha = 1.5$, the stable one corresponding to the larger value of R_1. Note that the plots of $g(R_1/R_2)$ for $\alpha = 10$ show the two analytically studied solution branches. (*b*) Plot of two helix segments on different cylinders. (Online version in colour.)

where the two branches meet is stable in R_1; (3) if there is one intersection with the upper curve, it is stable in R_1.

(ii) Comparison with data from a set of bacteriophages

We start exploring the parameters K_2, K_3, ν and σ of the model. Following Tzlil *et al.* [44], we express

$$K_3 = K_B T L_p m_0, \tag{3.45}$$

where K_B is the Boltzmann constant, T the absolute temperature, m_0 represents the linear density of DNA in the capsid and L_p the persistence length. The quantity m_0 represents the linear density of DNA in the capsid and has dimensions of square inverse of the length. Table 1 lists the value of m_0 for a sample of four viruses. For instance, for T4, we estimate $m_0 = 1/(\pi(d_0/2)^2) = 0.221\ \text{nm}^{-2}$ ($d_0 \approx 2.4\,\text{nm}$), and taking $T = 300\,\text{K}$ gives

$$K_3 = 5 \times 10^{-11}\,\text{J m}^{-1}. \tag{3.46}$$

In [27], we take guidance from the theory of Onsager for lyotropic liquid crystals, to obtain expressions for the isotropic modulus ν and the surface tension σ, and assume that they are functions of the (DNA) molar concentration c [45]. We adopt the expressions

$$\nu = \nu_0(c)\frac{K_B T}{R_2^3} \quad \text{and} \quad \sigma = \sigma_0(c)\frac{K_B T}{L_p d_0}. \tag{3.47}$$

Since, to our knowledge, no molecular theory is available to determine the dimensionless parameters ν_0 and σ_0, and, likewise, we do not have an expression for K_2 either, we proceed to estimate these three quantities from the data shown in the table. (The analogous approach followed in [27], and taking the capsid to be a sphere with the DNA arranged in concentric circles, gives $\nu_0 = 23$ and $\sigma_0 = 0.388$.)

Prior to estimating ν_0 and σ_0, and taking into account that for DNA $\alpha > 1$ holds, the stability properties listed in §3d(i) indicate that the solution R_1 in the graphs shown in figure 3 lies either on the *concentric circle* branch or on the monotonically decreasing portion corresponding to $\alpha = 10$. Moreover, as the experimental values of R_1/R_2 shown in table 1 indicate, the solutions for the viruses T4, T7 and $\epsilon 15$ are located in the latter branch, whereas that for T5 belongs to the concentric circle one. Also, for $\alpha = 10$, the largest possible value of R_1 is where the blue and red curves meet. The results for $\alpha = 10$ generalize to the case that α is large: the graph of $g(\cdot)$ has two branches, with the system having a stable helical configuration corresponding to the

Downloaded from https://royalsocietypublishing.org/ on 05 October 2022

Table 1. Physical measurements of four different bacteriophages [27]. The symbol L_p denotes the persistence length of a DNA chain of length L, effective diameter d_0, molar concentration c in a sphere-like capsid of radius R_c with a measured radius r_c of the disordered core. m_0 represents the linear density. T4 [2,3]; T5 [4]; T7 [1]; ϵ15 [5].

virus	L_p (nm)	d_0 (nm)	c	L (nm)	R_2 (nm)	R_1/R_2	m_0 (m^{-2})
T4	55.60	2.40	21.37	55047.6	40.00	0.5500	2.21×10^{17}
T5	58.38	2.94	17.85	39423.8	42.00	0.4286	1.47×10^{17}
T7	52.88	2.60	18.17	12932.0	26.05	0.5889	1.88×10^{17}
ϵ15	53.90	2.55	13.98	1284.6	28.37	0.5735	1.96×10^{17}

largest possible value of R_1. On the other hand, if $0 < \alpha$ is relatively small, such that $g(\cdot)$ has a single branch, then the stable configuration becomes $R_1 = 1$, with the inner capsid region being disordered.

In order to fit the curves with the experimental data of R_1/R_2 shown in table 1, we appeal to a scaling argument and estimate the value $\nu_0 \sim 500$ so that $\nu R_2^2/K_3 \sim 1$. With the appropriate choice of σ_0, this yields intersections between the straight line and the graph of $g(\cdot)$, in the stable range of the helical curves and the concentric-circle curves, at values $R_1/R_2 \approx 0.4 \sim 0.6$.

4. A filament reconstruction

In the previous sections, we have obtained a vector field $\boldsymbol{n}$, parameterized by the angle ψ that forms with the horizontal azimuthal vector $\boldsymbol{e}_\theta$ (3.3), that minimizes the total energy (3.40). In this section, we construct a smooth curve, a *filament*, that starting at a given point at the entrance of the capsid, remains tangent to $\boldsymbol{n}$ at every point. We recall the invariance property of nematic liquid crystals to the change $\pm\boldsymbol{n}$ that allows us to replace the oriented vector field with the corresponding line field.

We consider an achiral liquid crystal, with $\tau = 0$, in which case, if $\psi(r)$ is the minimizing angle $-\psi(r)$ is also an energy minimizer, with the same energy. Moreover, $\pm\psi$ represent the right- and left-handed helices, respectively. The reconstructed filament consists of piece-wise helical strands over cylinders of radius $r_i, i = 1, \ldots, N$, with same or alternate handedness and connected by interpolating smooth curves.

For a given $\epsilon > 0$, let the point $(r_1 = R_2 - \epsilon, \theta = 0, z = -h)$ represent the location where the DNA segment enters the capsid. The number ϵ is taken to be of the order of the capsid thickness, that we assume to be comparable with the effective diameter of the DNA filament d_0. The reconstruction of the centre axis of the DNA curve of length $L > 0$ inside a cylindrical capsid of radius R_2 and height $2h$ starts with the observation that the sub-filament of length $0 < L_1 \le L$ is organized in piece-wise helices over a discrete collection of cylinders of radius r_i,

$$\begin{aligned} &R_1 + \epsilon \le r_i \le R_2 - \epsilon, \quad i = 1, 2, \ldots, N, \\ &r_1 = R_2 - \epsilon, \quad r_2 = r_1 - d(r_1), \ldots, r_N = r_{N-1} - d(r_{N-1}), \end{aligned} \tag{4.1}$$

where N is a positive integer, and $d(r)$ is the pitch of the helix on the cylinder of radius $R_1 < r < R_2$, both to be determined. We also take the distance between two neighbouring cylinders of radius $r = r_i$ and $r = r_{i+1}$ to be $d(r_i)$, providing the same spacing as that between neighbouring segments of the helix on $r = r_i$. The core radius $R_1 > 0$, also resulting from the minimization problem, allows us to calculate N: from (4.1), N is the largest integer so that $r_{N+1} \le R_1$. The length of the ordered DNA is then

$$L_1 = \sum_{i=1}^{N} L_1^i + O(\epsilon), \tag{4.2}$$

Downloaded from https://royalsocietypublishing.org/ on 05 October 2022

where L_1^i is the length of the helix on the cylinder of radius r_i. The correction term in the above sum accounts for the length of the curves connecting the helical segments. The length of the disordered DNA is then $L_2 = L - L_1$.

Remark 4.1. We assume that the full genome is being packed, and it is sufficiently long to fill the entire capsid. Modelling the packing of a short genome should include the nematic order parameter that keeps track of the local DNA concentration.

Let $s \in (0, L_1)$ denote the arc length parameter of the DNA centre curve, $\boldsymbol{r} = \boldsymbol{r}(s)$. We recall that the vector field representation of a helix on the cylinder of radius $r > 0$, is given by the vector equation

$$\boldsymbol{r}(s) = r\boldsymbol{e}_r(\theta(s)) + z(\theta(s))\boldsymbol{e}_z, \quad s \in [s_i, s_{i+1}], \tag{4.3}$$

Here, $0 < s_i < s_{i+1} < L_1$ represents the arc length values such that $z(\theta(s_i)) = -h$ and $z(\theta(s_{i+1})) = h$, in the case that the curve is spooling along the positive z-direction, with the opposite signs otherwise. Furthermore, we seek $\boldsymbol{r}(s)$ such that, at the point corresponding to the cylindrical coordinates $(r_i, \theta(s), z(\theta(s)))$ is tangent to the vector field $\boldsymbol{n}$. That is, we require

$$\frac{\mathrm{d}\boldsymbol{r}}{\mathrm{d}s} = \boldsymbol{n}(\theta(s); r) = \cos\psi(r)\boldsymbol{e}_\theta(\theta(s)) + \sin\psi(r)\,\boldsymbol{e}_z \tag{4.4}$$

and

$$s \in [s_i, s_{i+1}], \quad \boldsymbol{r}(s_i) = r_i\boldsymbol{e}_r. \tag{4.5}$$

Calculating

$$\frac{\mathrm{d}\boldsymbol{r}}{\mathrm{d}s} = \frac{\mathrm{d}\boldsymbol{r}}{\mathrm{d}\theta}\frac{\mathrm{d}\theta}{\mathrm{d}s} = \left(r\boldsymbol{e}_\theta + \frac{\mathrm{d}z}{\mathrm{d}\theta}\boldsymbol{e}_z\right)\frac{\mathrm{d}\theta}{\mathrm{d}s}, \tag{4.6}$$

and combining it with (4.5), we obtain

$$\frac{\mathrm{d}\theta}{\mathrm{d}s} = \frac{1}{r}\cos\psi(r) \quad \text{and} \quad \frac{\mathrm{d}z}{\mathrm{d}\theta}\frac{\mathrm{d}\theta}{\mathrm{d}s} = \sin\psi. \tag{4.7}$$

Integrating the latter on the surface of cylinder of radius r, $R_1 < r < R_2$, we obtain

$$\theta(s) = \frac{s}{r}\cos\psi(r) + C_1 \quad \text{and} \quad z(s) = s\sin\psi(r) + C_1 r\tan\psi(r) + C_2, \tag{4.8}$$

where C_1 and C_2 are arbitrary constants.

Remark 4.2. In the special case of $R_1 = 0$, equation (3.23), we get

$$\theta(s) = 2\frac{R_2}{r^2 + R_2^2}s \quad \text{and} \quad z(s) = \frac{R_2^2 - r^2}{R_2^2 + r^2}s. \tag{4.9}$$

Note that, in calculating $\sin\psi$ from its cosine, we have chosen the positive sign, this being consistent with the convention that the curve starts at $z = 0$ and it spirals towards the positive z-axis.

Next, with a simple calculation, we get the pitch d of the helix in (4.8). Let us consider a point of the helix on the cylinder of radius r corresponding to the arc length $s > 0$, and a second point on the same helix but at the location $s + l$, $l > 0$. We let $l > 0$ and $d > 0$ be such that

$$\theta(s + l) = \theta(s) + 2\pi \quad \text{and} \quad z(\theta(s + l)) = z(\theta(s)) + d(r). \tag{4.10}$$

The latter, together with equations (4.8), gives $d(r) = l\sin\psi(r)$ and $l = 2\pi r\sec\psi$. Hence

$$d(r) = 2\pi r\tan\psi(r). \tag{4.11}$$

The plots in figure 1*a* show that $\psi(r)$ is very small (near 0) for r close to R_2. This indicates that the outer cylindrical layers have a higher filament concentration (since a decrease in $d(r)$ represents tighter coiling) than the inner ones, as consistently shown in experiments. Also, from figure 1*a*, we see that the overall values of ψ decrease as K_2 increases, that is the angles are smaller for higher twist energy penalty, also to be expected.

Downloaded from https://royalsocietypublishing.org/ on 05 October 2022

We obtain the equation of the centreline curve on subsequent cylindrical layers, located at $r_1, r_2, \ldots, r_N$, respectively. The independent segments in each cylinder are connected by interpolating lines, $\mathcal{U}$-turns, mimicking inter-layered spooling curves, resulting in a globally smooth curve.

The reconstructed DNA centre line is a piece-wise smooth helical curve, consisting of ordered strands as in (4.6) and (4.8) connected by interpolating segments.

First layer. Assuming that the DNA is spooled counterclockwise from the location $r = r_1$ near the capsid inner wall to the inner core, the first segment corresponds to equations (4.8) subject to the initial conditions

$$\theta(0) = 0 \quad \text{and} \quad z(0) = -h, \quad s_0 := 0, \tag{4.12}$$

i.e.

$$\theta(s) = \frac{s}{r_1}\cos\psi(r_1) \quad \text{and} \quad z(s) = \sin\psi(r_1)s - h. \tag{4.13}$$

We have seen in the previous sections that for the energy minimizing vector field $0 \le \psi(r) \le (\pi/2)$ for $r \in [R_1, R_2]$, with $\psi(r) \neq 0$ for $r < R_2$. This guarantees $\sin\psi(r) \neq 0$, for $r < R_2$. Note that the curve (4.3) and (4.13) reaches the top of the capsid $z = h$ for s such that

$$s = \frac{2h}{\sin\psi(r_1)} := s_1. \tag{4.14}$$

We observe that the quantity s_1 gives the length of the helix segment, on the surface of the cylinder $r = r_1$, running from $z = -h$ to $z = h$. Furthermore, let us denote

$$\theta_1 = \theta(s_1) \quad \text{and} \quad P_1 := (r_1, \theta_1, h). \tag{4.15}$$

Second layer. The second layer, the cylinder of radius $r_2 = r_1 - d(r_1)$, is covered by the helix (4.8) with angle $\psi(r_2)$. The initial point is $P_2 = (r_2, \theta_2, h - d(r_1))$, with θ_2 determined according to the *connection condition* established next. So, the helical segment corresponds to the curve (4.8), with $r = r_2$ and $\theta \le \theta_2$, up to reaching $z = -h$.

Connecting layer. We construct an interpolating curve that joins the DNA segments on two consecutive cylinders, from the outer to the inner one. The construction of the connecting layer segments is shown in the electronic supplementary material section.

5. Conclusion

We have presented a model of packaged DNA in a cylindrical capsid based on the duality of the vector field and filament approach. We have shown that the model includes fundamental features, some of them encountered in separate earlier models, such as the hexagonal crystal structure of DNA cross sections. Our work also generalizes the inverse spooling assumption that has been key to earlier research and replaces it with fully helical configurations of the vector field able to sustain both twist and bending.

The main results of the work can be summarized as follows. First of all, by considering a cylindrical domain, we find that divergence-free solutions of the vector field are axisymmetric, depending only on the radial coordinate. In the achiral case $\tau = 0$, we study two types of boundary value problems, one with a fixed inner core of radius $R_1 \ge 0$ (§3b), and one with an unknown inner core (§3d). In the latter case, an isotropic energy penalty of the disordered core is included, leading to a free boundary problem. There exist solutions corresponding to concentric circles and helical vector fields (with both signs of the director angle, $\pm\psi(r)$). The latter solutions are studied in §3b and classified according to the value of the parameter α, the ratio between the bending and twist moduli. Section 3(c) is devoted to the stability analysis of the helical solutions (theorem 3.7), and that of the concentric circles (theorem 3.8). Sufficient conditions for their stability are formulated in terms of the two main parameter values, α and the ratio R_2/R_1 of the capsid radius and that of the fixed inner core. Pairs of helical solutions are also found in the chiral case. The article concludes with a reconstruction of the filament from the helical vector field.

Downloaded from https://royalsocietypublishing.org/ on 05 October 2022

The assumption of Dirichlet boundary conditions on the capsid wall may be unreasonably restrictive and possibly misrepresent the role of the proteins there. In future work, we will relax it by assigning an anchoring energy to the capsid wall. Furthermore, in the case that such an energy is anisotropic, it may allow for corners and facets, consistent with the icosahedral geometry of the capsid. For simplicity, we do not incorporate the scalar order parameter variable of our earlier work that helps quantify the density of the DNA [24]. The work presented here is purely mechanical with no electrostatic contributions of the DNA and the environmental ions taken into account as done in our previous work [25]. The latter issues as well as the extension to capsid shapes other than cylindrical can be computationally accomplished by numerical techniques. Finally, we point out the ideal nature of the reconstructed filament in that it does not account for knots. This issue is the subject of follow up work.

Data accessibility. This article has no additional data.

Authors' contributions. P.L.: formal analysis, investigation, methodology, writing—original draft, writing—review and editing; J.A.: conceptualization, methodology, writing—review and editing; M.C.C.: conceptualization, formal analysis, methodology, project administration, supervision, writing—original draft, writing—review and editing; D.G.: formal analysis, methodology, writing—review and editing; M.V.: conceptualization, methodology, writing—review and editing; S.W.: formal analysis, methodology, writing—review and editing.

All authors gave final approval for publication and agreed to be held accountable for the work performed therein.

Conflict of interest declaration. We declare that we have no competing interests.

Funding. This work was partially supported by National Science Foundation grant nos. DMS-1817156 (J.A. and M.V.), DMS-1816740 (M.C.C. and P.L.), DMS-1729538 (D.G.) and DMS-1555222-CAREER, DMS-2111474 (S.W.).

References

1. Cerritelli ME, Cheng N, Rosenberg AH, McPherson CE, Booy FP, Steven A. 1997 Encapsidated conformation of bacteriophage T7 DNA. *Cell* **91**, 271–280. (doi:10.1016/S0092-8674(00)80409-2)
2. Olson NH, Gingery M, Eiserling FA, Baker TS. 2001 The structure of isometric capsids of bacteriophage T4. *Virology* **279**, 385–391. (doi:10.1006/viro.2000.0735)
3. Mesyanzhinov VV. 2004 Bacteriophage T4: structure, assembly, and initiation infection studied in three dimensions. *Adv. Virus Res.* **63**, 287–352. (doi:10.1016/S0065-3527(04)63005-3)
4. Effantin G, Boulanger P, Neumann E, Letellier L, Conway JF. 2006 Bacteriophage T5 structure reveals similarities with HK97 and T4 suggesting evolutionary relationships. *J. Mol. Biol.* **361**, 993–1002. (doi:10.1016/j.jmb.2006.06.081)
5. Jiang W, Chang J, Jakana J, Weigele P, King J, Chiu W. 2006 Structure of epsilon15 bacteriophage reveals genome organization and DNA packaging/injection apparatus. *Nature* **439**, 612–616. (doi:10.1038/nature04487)
6. Guo F *et al.* 2014 Capsid expansion mechanism of bacteriophage T7 revealed by multistate atomic models derived from cryo-EM reconstructions. *Proc. Natl Acad. Sci. USA* **111**, E4606–E4614. (doi:10.1073/pnas.140702011)
7. Huet A, Duda RL, Boulanger P, Conway JF. 2019 Capsid expansion of bacteriophage T5 revealed by high resolution cryoelectron microscopy. *Proc. Natl Acad. Sci. USA* **116**, 21 037–21 046. (doi:10.1073/pnas.1909645116)
8. Lomonossoff GP, Wege C. 2018 TMV particles: the journey from fundamental studies to bionanotechnology applications. *Adv. Virus Res.* **102**, 149–176. (doi:10.1016/bs.aivir.2018.06.003)
9. Leforestier A. 2013 Polymorphism of DNA conformation inside the bacteriophage capsid. *J. Biol. Phys.* **39**, 201–213. (doi:10.1007/s10867-013-9315-y)
10. Leforestier A, Livolant F. 2010 The bacteriophage genome undergoes a succession of intracapsid phase transitions upon DNA ejection. *J. Mol. Biol.* **396**, 384–395. (doi:10.1016/j.jmb.2009.11.047)
11. Lepault J, Dubochet J, Baschong W, Kellenberger E. 1987 Organization of double-stranded DNA in bacteriophages: a study by cryo-electron microscopy of vitrified samples. *EMBO J.* **6**, 1507–1512. (doi:10.1002/j.1460-2075.1987.tb02393.x)

Downloaded from https://royalsocietypublishing.org/ on 05 October 2022

12. Livolant F, Levelut AM, Doucet J, Benoit JP. 1989 The highly concentrated liquid-crystalline phase of DNA is columnar hexagonal. *Nature* **339**, 724–726. (doi:10.1038/339724a0)
13. Strzelecka TE, Davidson MW, Rill RL. 1988 Multiple liquid crystal phases of DNA at high concentrations. *Nature* **331**, 457–460. (doi:10.1038/331457a0)
14. Earnshaw WC, King J, Harrison SC, Eiserling FA. 1978 The structural organization of DNA packaged within the heads of T4 wild-type, isometric and giant bacteriophages. *Cell* **14**, 559–568. (doi:10.1016/0092-8674(78)90242-8)
15. Purohit PK, Kondev J, Phillips R. 2003 Mechanics of DNA packaging in viruses. *Proc. Natl Acad. Sci. USA* **100**, 3173–3178. (doi:10.1073/pnas.0737893100)
16. Hud NV. 1995 Double-stranded DNA organization in bacteriophage heads: an alternative toroid-based model. *Biophys. J.* **69**, 1355–1362. (doi:10.1016/S0006-3495(95)80002-0)
17. Earnshaw WC, Harrison SC. 1977 DNA arrangement in isometric phage heads. *Nature* **268**, 598–602. (doi:10.1038/268598a0)
18. Purohit PK, Kondev J, Phillips R. 2003 Force steps during viral DNA packaging? *J. Mech. Phys. Solids* **51**, 2239–2257. (doi:10.1016/j.jmps.2003.09.016)
19. Kindt J, Tzlil S, Ben-Shaul A, Gelbart WM. 2001 DNA packaging and ejection forces in bacteriophage. *Proc. Natl Acad. Sci. USA* **98**, 13 671–13 674. (doi:10.1073/pnas.241486298)
20. Arsuaga J, Tan R, Vazquez M, Harvey SS. 2002 Investigation of viral DNA packaging using molecular mechanics models. *Biophys. Chem.* **101**, 475–484. (doi:10.1016/S0301-4622(02)00197-7)
21. Casjens SR. 2011 The DNA packaging nanomotor of tailed bacteriophages. *Nat. Rev. Microbiol.* **9**, 647–657. (doi:10.1038/nrmicro2632)
22. Petrov AS, Boz MB, Harvey SC. 2007 The conformation of double-stranded DNA inside bacteriophages depends on capsid size and shape. *J. Struct. Biol.* **160**, 241–248. (doi:10.1016/j.jsb.2007.08.012)
23. Petrov AS, Lim-Hing K, Harvey SC. 2007 Packaging of DNA by bacteriophage epsilon15: structure, forces, and thermodynamics. *Structure* **15**, 807–812. (doi:10.1016/j.str.2007.05.005)
24. Walker S, Arsuaga J, Hiltner L, Calderer MC, Vazquez M. 2020 Fine structure of viral dsDNA encapsidation. *Phys. Rev. E* **101**, 022703. (doi:10.1103/PhysRevE.101.022703)
25. Liu P, Arsuaga J, Calderer MC, Golovaty D, Vazquez M, Walker S. 2021 Ion-dependent DNA configuration in bacteriophage capsids. *Biophys. J.* **120**, 3292–3302. (doi:10.1016/j.bpj.2021.07.006)
26. Klug WS, Ortiz M. 2003 A director-field model of DNA packaging in viral capsids. *J. Mech. Phys. Solids* **51**, 1815–1847. (doi:10.1016/S0022-5096(03)00071-1)
27. Hiltner L, Calderer MC, Arsuaga J, Vázquez M. 2021 Chromonic liquid crystals and packing configurations of bacteriophage viruses. *Phil. Trans. R. Soc. A* **379**, 20200111. (doi:10.1098/rsta.2020.0111)
28. Hang F, Lin F, Yang Y. 2008 Existence of Faddeev knots. *Surv. Differ. Geometry* **13**, 149–222. (doi:10.4310/SDG.2008.v13.n1.a6)
29. Shin H, Grason GM. 2011 Filling the void in confined polymer nematics: phase transitions in a minimal model of dsDNA packing. *Europhys. Lett.* **96**, 36007. (doi:10.1209/0295-5075/96/36007)
30. Lucchetti L, Fraccia TP, Nava G, Turiv T, Ciciulla F, Bethge L, Klussmann S, Lavrentovich OD, Bellini T. 2020 Elasticity and viscosity of dna liquid crystals. *ACS Macro Lett.* **9**, 1034–1039. (doi:10.1021/acsmacrolett.0c00394)
31. Bethuel F, Brezis H, Coleman BD, Hélein F. 1992 Bifurcation analysis of minimizing harmonic maps describing the equilibrium of nematic phases between cylinders. *Arch. Ration. Mech. Anal.* **118**, 149–168. (doi:10.1007/BF00375093)
32. Golovaty D, Kim Y, Lavrentovich OD, Novack M, Sternberg P. 2020 Phase transitions in nematics: textures with tactoids and disclinations. *Math. Model. Nat. Phenomena* **15**, 8. (doi:10.1051/mmnp/2019034)
33. Relaix S, Mitov M. 2008 Polymer-stabilised cholesteric liquid crystals with a double helical handedness: influence of an ultraviolet light absorber on the characteristics of the circularly polarised reflection band. *Liq. Cryst.* **35**, 1037–1042. (doi:10.1080/02678290802364020)
34. Gaill F, Bouligand Y. 1987 Alternating positive and negative twist of polymers in an invertebrate integument. *Mol. Cryst. Liq. Cryst.* **153**, 31–41. (doi:10.1006/viro.2000.0735)
35. Katsonis N, Lacaze E, Ferrarini A. 2012 Controlling chirality with helix inversion in cholesteric liquid crystals. *J. Mater. Chem.* **22**, 7088–7097. (doi:10.1039/c2jm15962g)

36. Zandi R, Dragnea B, Travesset A, Podgornik R. 2020 On virus growth and form. *Phys. Rep.* **847**, 1–102. (doi:10.1016/j.physrep.2019.12.005)
37. Svenšek D, Podgornik R. 2013 Confined chiral polymer nematics: ordering and spontaneous condensation. *Europhys. Lett.* **100**, 66005. (doi:10.1209/0295-5075/100/66005)
38. Svenšek D, Veble G, Podgornik R. 2010 Confined nematic polymers: order and packing in a nematic drop. *Phys. Rev. E* **82**, 011708. (doi:10.1103/PhysRevE.82.011708)
39. Curk T, Farrell J, Dobnikar J, Podgornik R. 2019 Spontaneous domain formation in spherically confined elastic filaments. *Phys. Rev. Lett.* **123**, 047801. (doi:10.1103/PhysRevLett.123.047801)
40. Hardt R, Kinderlehrer D, Lin FH. 1986 Existence and partial regularity of static liquid crystal configurations. *Commun. Math. Phys.* **105**, 547–570. (doi:10.1007/BF01238933)
41. Hale JK. 1980 *Ordinary differential equations*. New York, NY: Krieer.
42. Black LW, Newcomb WW, Boring JW, Brown JC. 1985 Ion etching bacteriophage T4: support for a spiral-fold model of packaged DNA. *Proc. Natl Acad. Sci. USA* **82**, 7960–7964. (doi:10.1073/pnas.82.23.7960)
43. Williams C, Pierański P, Cladis PE. 1972 Nonsingular $s = +1$ screw disclination lines in nematics. *Phys. Rev. Lett.* **29**, 90–92. (doi:10.1103/PhysRevLett.29.90)
44. Tzlil S, Kindt JT, Gelbart WM, Ben-Shaul A. 2003 Forces and pressures in DNA packaging and release from viral capsids. *Biophys. J.* **84**, 1616–1627. (doi:10.1016/S0006-3495(03)74971-6)
45. Onsager L. 1949 The effects of shape on the interaction of colloidal particles. *Ann. NY Acad. Sci.* **51**, 627–659. (doi:10.1111/j.1749-6632.1949.tb27296.x)

Downloaded from https://royalsocietypublishing.org/ on 05 October 2022